

# Mapping the Origins of Luminescence in ZnO Nanowires by STEM-CL

Oscar W. Kennedy,<sup>†,‡,§,||</sup> Edward R. White,<sup>§,||</sup> Ashley Howkins,<sup>||</sup> Charlotte K. Williams,<sup>⊥,||</sup> Ian W. Boyd,<sup>||</sup> Paul A. Warburton,<sup>†,‡</sup> and Milo S. P. Shaffer<sup>\*,§,⊗,||</sup>

<sup>†</sup>London Centre for Nanotechnology, University College London, London WC1H 0AH, United Kingdom

<sup>‡</sup>Department of Electronic and Electrical Engineering, University College London, London WC1E 7JE, United Kingdom

<sup>§</sup>Department of Chemistry, Imperial College London, London SW7 2AZ, United Kingdom

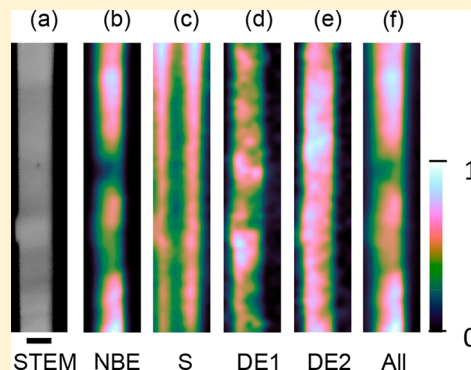
<sup>||</sup>Experimental Techniques Centre, Brunel University London, Uxbridge UB8 3PH, United Kingdom

<sup>⊥</sup>Department of Chemistry, Oxford University, Oxford OX1 3TA, United Kingdom

<sup>⊗</sup>Department of Materials, Imperial College London, London, SW7 2AZ, United Kingdom

## S Supporting Information

**ABSTRACT:** In semiconductor nanowires, understanding both the sources of luminescence (excitonic recombination, defects, etc.) and the distribution of luminescent centers (be they uniformly distributed, or concentrated at structural defects or at the surface) is important for synthesis and applications. We develop scanning transmission electron microscopy–cathodoluminescence (STEM-CL) measurements, allowing the structure and cathodoluminescence (CL) of single ZnO nanowires to be mapped at high resolution. Using a CL pixel resolution of 10 nm, variations of the CL spectra within such nanowires in the direction perpendicular to the nanowire growth axis are identified for the first time. By comparing the local CL spectra with the bulk photoluminescence spectra, the CL spectral features are assigned to internal and surface defect structures. Hyperspectral CL maps are deconvolved to enable characteristic spectral features to be spatially correlated with structural features within single nanowires. We have used these maps to show that the spatial distribution of these defects correlates well with regions that show an increased rate of nonradiative transitions.



Zinc oxide (ZnO) offers a number of attractive features relevant to application, including a wide band gap, optical transparency, large exciton binding energy, and earth-abundant elemental composition.<sup>1</sup> ZnO nanowires, in particular, have shown promise in optoelectronics,<sup>2</sup> lasers,<sup>3</sup> photovoltaics,<sup>4</sup> and gas sensing.<sup>5</sup> However, defects can dictate nanowire device performance: surface states cause band bending and deplete the carrier density,<sup>6,7</sup> whereas optically active defects provide unwanted recombination routes. The density and distribution of these defects, as well as the length scale over which they influence properties, are important practical considerations both for applications where surface interactions are critical (e.g., photocatalysis and chemical sensing<sup>8–11</sup>) and more generally for ZnO nanodevices.

Extensive work on ZnO photo- and cathodo-luminescence (PL and CL respectively) has identified a number of spectral contributions.<sup>12</sup> Primary luminescence signals arise from transitions across the band gap often mediated by excitons,<sup>12</sup> and transitions are associated with a variety of defects.<sup>13</sup> Impurity elements often play a crucial role, but even in elementally pure ZnO there are defect states that lie within the band gap and contribute to luminescence, include those arising at 2.0 eV (doubly charged O vacancies)<sup>14</sup> and 1.94 eV (O-rich

growth conditions or O interstitials).<sup>15,16</sup> In nanostructures, the external surface becomes particularly significant and may be associated with different types (or concentrations) of defects compared with the core. Broad signals from such surface states in nanostructures have previously been observed by PL (at 2.4 to 2.54 eV<sup>17–19</sup> and 2.2 eV<sup>20</sup> central energies) and monochromatic CL (2.5 eV)<sup>21</sup> in ZnO nanostructures. Despite progress, the assignments of spectral features to specific structures are often uncertain, and a combined understanding of both the spatial distribution and the spectral variation of defects remains elusive.

An ideal technique for characterizing defect states in nanostructures would combine spatially resolved emission measurements with high-resolution structural imaging. Here, we describe scanning transmission electron microscopy–cathodoluminescence<sup>22–24</sup> (STEM-CL) measurements of individual high-quality ZnO nanowires. Existing efforts to study ZnO luminescence using SEM-CL<sup>25,26</sup> suffer from large electron-beam interaction volumes, which limit resolution; CL

Received: October 29, 2018

Accepted: January 6, 2019

Published: January 7, 2019

emission has only been mapped longitudinally along single ZnO nanowires. The characteristics in directions normal to the growth axis have not been resolved, although they are critical for both a fundamental understanding and a number of device applications. STEM-CL has not been widely applied to such systems, although it has previously been used to map CL from quantum wells in GaN nanowires<sup>27</sup> and collect localized CL spectra from ZnO tetrapods<sup>28</sup> and 1D hyperspectral line scans on single GeS nanosheets.<sup>29</sup>

Here, by using STEM-CL, we have deconvoluted the spatial variation of the CL spectra arising from the nanowire core, the nanowire surface, and internal defects. The high-energy electron probe used in STEM affords simultaneous structural imaging with local excitation of electron–hole pairs. The spectrum of light emitted by radiative recombination is recorded as the electron beam rasters the nanowire. The resulting high-resolution maps correlate the CL spectra with the nanowire geometry and hence help to identify the origin of optical traps in individual nanowires.

Samples were prepared as described in the [Supporting Information \(SI\)](#). STEM-CL data were acquired with a Gatan Vulcan CL system in a JEOL 2100 field-emission scanning TEM operated at 80 kV with a 1 nA beam current and a 1 nm spot size. A pair of mirrors mounted on the sample holder focused the emitted light onto optical fibers that fed an optical spectrometer. CL spectra were recorded, one at each pixel rastered by the electron beam (10 nm pixel size, 3 s dwell time resulting in an electron dose of  $30 \mu\text{C}/\mu\text{m}^2$ ), with  $16 \times 16$  subpixel scanning enabled. These imaging conditions were chosen to maximize the CL signal and spatial resolution while minimizing damage to the nanowire structure. To enhance radiative recombination and minimize knock-on damage, the nanowires were liquid-nitrogen-cooled to a temperature of 103 K. PL was performed at room temperature using a He/Cd laser with an excitation wavelength of 325 nm using a Renishaw fluorescence microscope.

High-quality ZnO nanowires were grown by molecular beam epitaxy on *c*-plane sapphire using a procedure reported previously<sup>30</sup> (see the SI for details). A TEM image of a typical nanowire ([Figure 1a](#)) shows a wurtzite crystal structure with a growth axis along the [0001] direction with atomic planes shown in [Figure 1b](#). The cross section of these

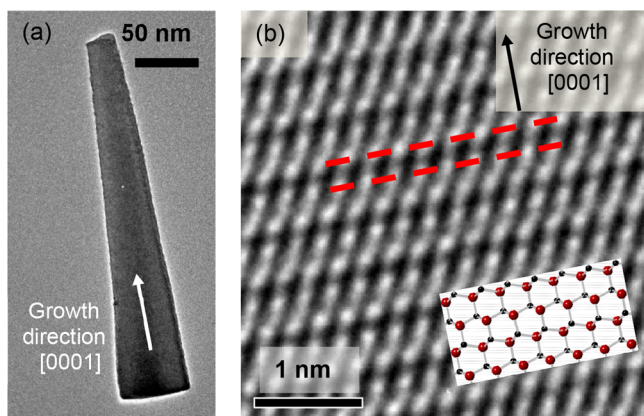


**Figure 1.** (a) TEM image of a ZnO nanowire. (b) High-resolution TEM micrograph showing the wurtzite ZnO structure with a growth axis along the [0001] direction and a 2.6 Å lattice spacing indicated by the dashed red lines. A reconstruction of the ZnO lattice is overlaid where Zn (O) atoms are blue (red).

nanowires varies from nanowire to nanowire due to local variations on the substrate during growth. [Figure 2a](#) shows a high-angle annular dark-field (HAADF) STEM image of a portion of a ZnO nanowire ( $\sim 60$  nm wide) where a hyperspectral CL image ( $51 \times 10$  spatial pixels) was acquired. With uniform composition, the HAADF signal can be taken as a measurement of local thickness, constraining the possible nanowire cross sections. The approximately uniform HAADF intensity across the direction normal to the nanowire shows that its thickness does not vary significantly, consistent, for example, with a near-rectangular section (see [Figure S11](#)). To determine the CL signal generated from defects, the electron beam was held at one spot to locally induce knock-on damage (i.e., vacancies) in the crystal lattice<sup>31</sup> for  $\sim 10$  s, resulting in a dose over two orders of magnitude higher than CL imaging. This location can be seen in the HAADF image ([Figure 2a](#)) as a dark spot approximately half way along the nanowire, as indicated by the arrow. There is a protrusion on the left side of the nanowire that may have been initiated by a defect occurring during growth; in this case, due to the axial growth direction, the defect should be localized toward the bottom of the protrusion, as observed. For other nanowires, we performed HRTEM prior to CL and found that nanowires that had been imaged showed reduced CL intensity in subsequent measurements compared with unexposed structures despite limiting dose and use of a cryo-holder. Conversely, HRTEM performed after STEM-CL acquisition is hindered by amorphous carbon deposition during STEM and potentially other STEM damage artifacts. In less sensitive materials, or with further detector refinement, atomic resolution spatial imaging might be combined with CL; here we focused on maximizing the resolution of the CL maps.

[Figure 2b](#) shows three archetypical spectra from the nanowire interior (red), near the base of the protrusion on the left side of the nanowire (green), and just outside the nanowire edge using an aloof beam condition<sup>32–34</sup> (blue). The interior and protrusion spectra both have a near-band-edge (NBE) emission peak centered at 3.4 eV (370 nm), consistent with the range of band gaps widely reported for both bulk ZnO and ZnO nanowires.<sup>35–37</sup> This band gap is in close agreement with the room-temperature PL data ([Figure 2m](#)), where increases in PL peak energy with decreasing temperature have been previously reported.<sup>38</sup> At lower energies there are small differences between the spectrum collected at the protrusion that has a broad low intensity peak in the range 1.8 to 2.5 eV compared with the bulk spectrum collected far away from any defects visible in the HAADF, for which this peak is either weaker or not present at all. Given the similar intensity in the two spectra from 2.5 to 3.0 eV, this difference is likely to be significant, as confirmed by the further analysis below. The aloof beam spectrum (referred to as S luminescence) is likely caused by surface states and is strongest in the blue, with a peak in counts at  $\sim 3$  eV. The aloof spectrum was fitted with a Gaussian after applying a Jacobian transformation (see [Figures S12 and S13](#) for fits), giving a central energy of 2.5 eV, consistent with energies previously reported for surface states.<sup>17–21</sup> This range of spectral features (in particular, the differing surface and bulk luminescence) was observed in multiple nanowires, including nanowires from a different growth run and nanowires measured on different days, as shown in [Figure S14](#).

To investigate the spatial dependence of the different luminescence signals, the CL intensity maps were summed

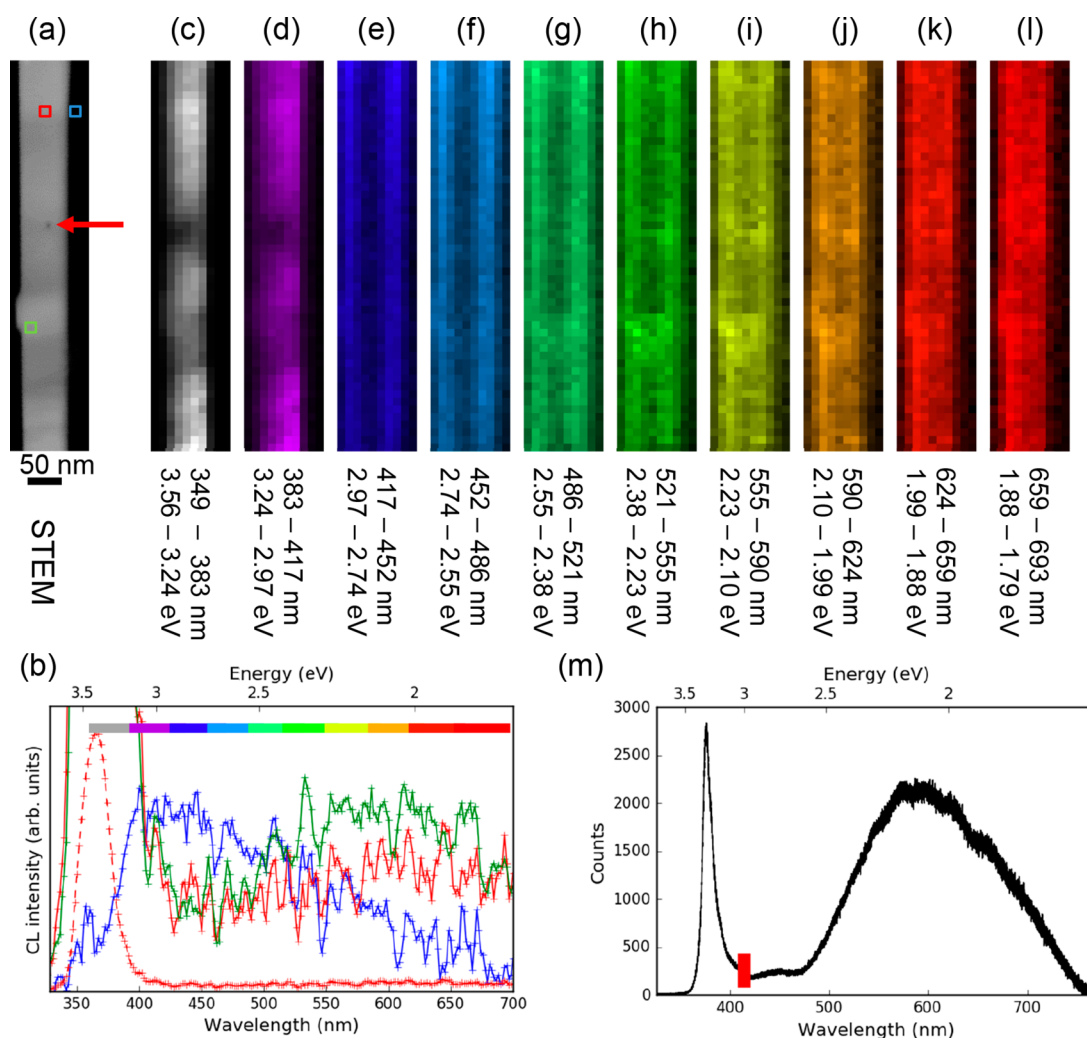


**Figure 2.** (a) HAADF STEM image of a ZnO nanowire. A dark spot where the electron beam was held to induce damage is indicated by the red arrow. (b) CL spectra acquired with the electron beam positioned in the nanowire's interior (red, where the solid line is the dashed scaled by a factor of 15), outside the nanowire (blue), and near the protrusion (green). Line colors correspond to the locations shown by the boxes in panel a. A five-point moving average is applied. Each spectrum is normalized separately for display purposes. (c–l) CL intensity maps generated from a hyperspectral CL image acquired over panel a with a pixel size of 10.2 nm. The brightness in each pixel is proportional to the CL integrated intensity across the wavelength/energy range indicated below each map, as shown in the color bar in panel b. Each map is normalized to the most intense pixel and colored according to the visible spectrum and its respective mean wavelength (UV is shown grayscale). (m) PL spectrum from a ZnO nanowire ensemble. The thick red line indicates a break between two spectra collected using different filters.

over consecutive wavelength/energy ranges (Figure 2c–l). By comparing these maps with the HAADF STEM image (Figure 2a), it is clear that the CL intensity varies across the nanowire in a strongly energy-dependent fashion, which must relate to different physical emission processes. On the basis of these maps, there appear to be four distinct spectral components. The UV/purple emission is strongest along the central axis of the nanowire, the blue emission is strongest at the nanowire surface, the green/yellow emission is strongest at the bottom of the protrusion (the likely location of a defect) in the nanowire, and low-energy red emission is present throughout the nanowire. Ensemble PL measures emission due to recombination via the same mechanisms as CL spectra and can therefore be used in tandem to assist interpretation.<sup>27</sup>

PL measurements on an ensemble of ZnO nanowires grown under similar conditions (Figure 2m) provide high signal-to-noise ratio (SNR) averaged data that confirm the identification of the separate components. The relative amplitudes of the NBE and defect emission peaks differ between the PL (Figure

2m) and CL (Figure 2b). The altered ratio may simply be due to the ensemble averaging in PL measurements of different quality nanostructures (with slightly different luminescence properties) but may also be fundamentally affected by the local excitation rate. The intensity of defect PL (relative to NBE PL) has been shown to decrease with increasing PL pump intensity as defects saturate.<sup>39</sup> As such, the high pump intensity of the very narrow STEM beam may cause the reduced amplitude of defect peaks in CL spectra. A study of STEM-CL at reduced beam currents would be interesting but is currently limited by CL detector efficiency. Recent work on SnO<sub>2</sub> nanowires<sup>23</sup> has also identified differences between PL and STEM-CL spectra; these effects were attributed either to low-quality polycrystalline SnO<sub>2</sub> byproducts or more directly to the dependence of the recombination route on excitation mechanisms. In the cited work on SnO<sub>2</sub>, a radial variation of CL signals (i.e., a reduction in the peak CL intensity at nanowire surfaces) was also reported, analogous to the reduction in ZnO NBE emission reported here. Spectral shifts on length scales of

10 nm were studied via linear scans across the diameter rather than mapped over the entire structure.

The PL spectrum (Figure 2m) has three obvious peaks: an intense NBE peak, a small peak at energies below the NBE peak (similar to S in CL spectra), and an intense peak in the green significantly more intense than the peak at similar energies seen in CL. The peak in the green requires a pair of Gaussians for a good fit (see Figure SI3), indicating that this lower energy peak is composed of at least two overlapping components and is fit here by two: defect emission 1 and 2 (DE1 and DE2). The central energy of surface luminescence S is close to that previously reported, with a similar breadth.<sup>17–21</sup> DE1 occurs at 2.1 eV, which has previously been associated with oxygen vacancies.<sup>14</sup> Emission at 1.8 eV (DE2) has been associated with Zn interstitials.<sup>40</sup>

Because the emission peaks are broad, each intensity map in Figure 2 includes contributions from multiple overlapping components. Therefore, to understand the correlation between CL emission and nanowire features, the hyperspectral CL image was deconvolved using four spectral components. Each CL spectrum was fitted to a linear superposition of the NBE, S, DE1, and DE2 peaks, where the energy and width of the distributions were fixed according to fits from the CL (NBE and S) and PL (DE1 and DE2) spectra<sup>41</sup> (see Figures SI2 and SI3 and Table 1). Although room-temperature PL is used to fit

**Table 1. Fit Results for Central Energy ( $E_0$ ) and Peak Width ( $\sigma$ ) of the Four Components Used To Deconvolve CL Spectra<sup>a</sup>**

component	PL/CL	$E_0$ (eV)	$\sigma$ (eV)
NBE	CL (103 K)	$3.40 \pm 0.01$	$0.106 \pm 0.001$
S	CL (103 K)	$2.53 \pm 0.05$	$0.61 \pm 0.05$
DE1	PL (300 K)	$2.08 \pm 0.01$	$0.194 \pm 0.001$
DE2	PL (300 K)	$1.82 \pm 0.01$	$0.091 \pm 0.001$

<sup>a</sup>Second column denotes whether CL or PL data were used to fit to the peaks and the temperature at which these measurements were performed. Fits were performed on data transformed into counts/eV (see the SI for details).

defect peaks, the temperature dependence of the peak positions is expected to be weak; recent measurements of defect emission have shown only small shifts ( $\sim 0.1$  eV) between 300 and 100 K.<sup>42</sup> This deconvolution routine accurately accounts for the full hyperspectral CL image (Figure SI5) and allows amplitude maps of each component to be plotted (Figure 3b–e). The errors in the peak amplitudes from the deconvolution routine are mapped in Figure SI6. The errors in each peak are much lower than the amplitude of the fitted signal. Typically, the errors are  $<10\%$  of the signal and are much lower at regions of interest where the amplitude of the signal is high. Adding additional peaks to fit the broad defect peak in the PL increases the errors in the deconvolved maps due to overfitting the spectrum, further justifying the number of components used.

These deconvolved CL maps clarify the relationship between the CL components and structural features that is obscured by component mixing in the raw integrated maps (Figure 2). The NBE component (Figure 3b) is brightest along the central axis of the nanowire and is suppressed near the nanowire surface and at up to  $\sim 50$  nm from the bottom of the protrusion and beam-induced defects (a measure of the exciton diffusion length in this nanowire). Previous measurements<sup>43</sup> of

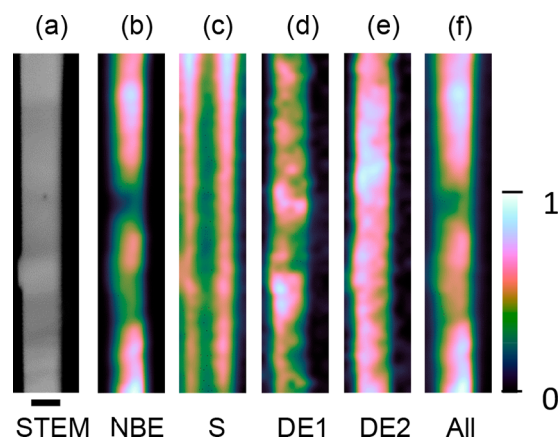


**Figure 3.** (a) HAADF STEM image of nanowire repeated from Figure 2a for reference. Scale bar is 50 nm. Amplitude maps of (b) near-band-edge emission, (c) surface emission, (d) defect emission 1, and (e) defect emission 2 deconvolved components. (f) Counts integrated across all energies. The intensity in each map is normalized and smoothed for presentation clarity by applying a Gaussian blur of pixels with a radius equal to half the CL pixel size (5.1 nm). To generate maps b–e, CL spectra are transformed to counts/eV and then fit. The amplitudes of these maps are 42 560, 2837, 2533, and 2981 respectively.

the exciton diffusion length, made by polychromatic SEM CL, were  $\sim 200$  nm in nanowires of 200 nm radius at 5 K<sup>44</sup> and  $\sim 100$  nm in a  $\sim 50$  nm diameter nanowire at 300 K. The NBE component is the dominant contribution to total CL intensity, exceeding the contributions of S, DE1, and DE2. Given the nanowire's uniform thickness profile (shown in Figure SI1), the surface suppression cannot be a thickness effect and must be related to competing recombination mechanisms. Similarly, alternative recombination routes explain the NBE suppression at the defects. The suppression of NBE emission shows that the exciton lifetime is longer than the lifetime associated with recombination across these defects.

Transient absorption spectroscopy on ZnO has shown rich recombination dynamics that vary even within single tapered nanowires.<sup>45</sup> In tapered nanowires, trap lifetimes are short at tips and longer in the core due to the effects of the cross section and available surface. Spatial resolution in single nanowires is achieved using confocal microscopy on large nanowires ( $\sim 2$   $\mu\text{m}$  maximum diameter and  $>10$   $\mu\text{m}$  long). These data are consistent with surface traps having shorter lifetimes than bulk traps, as indicated by our measurements. The same work showed that the lifetime of NBE emission was much shorter than the lifetime of trap states. Nevertheless, our measurements show that traps suppress NBE emission, which may indicate that although trap lifetimes are long, carrier trapping occurs on short time scales comparable to or faster than NBE emission.

The blue emission, labeled S (Figure 3c), is brightest at the nanowire surfaces and is therefore attributed to surface traps, previously ascribed to adsorbed oxygen,<sup>46</sup> Zn vacancies,<sup>47</sup> and neutral oxygen vacancies.<sup>17</sup> S emission occurs away from the nanowire surface extending both outside and inside the nanowire. The S signal is strongest at the edges, where the entire primary electron beam trajectory intersects with the surface region; in the center of the NW, the beam only intersects with the upper and lower surfaces. The significant S intensity when the electron beam is aloof (nearly but not

intersecting with the nanowire) is likely due to the excitation of surface plasmons,<sup>48,49</sup> which decay to excitons and subsequently recombine via surface traps in the ZnO, but may also be caused by stray electrons that directly excite excitons preferentially at the nanowire surface. The peak of S intensity extends into the nanowire due to excitons excited in the nanowire diffusing to the surface, where they subsequently decay. The yellow/green defect emission, DE1 (Figure 3d), is strongest near the two structural defects in the nanowire, the same regions where NBE is less intense. Far away from structural defects, the DE1 emission is nonzero, indicating that this trap is present throughout the nanowire but at higher concentrations around structural defects. DE1 is centered at 2.1 eV, and luminescence at this energy has previously been attributed to O vacancies,<sup>14</sup> consistent with vacancies induced by knock-on damage. DE1 is less intense at the surfaces of the nanowire, indicating that DE1 is slower than recombination due to surface states. The orange/red defect emission, DE2 (Figure 3e), has a central energy of 1.8 eV and is approximately uniform along the nanowire, with a small decrease at the nanowire surface, and occurs at energies previously associated with Zn interstitials,<sup>40</sup> although others<sup>50</sup> question whether Zn interstitials are stable in ZnO.

The total integral of the CL counts, mapped across the nanowire (Figure 3f), highlights the occurrence of nonradiative recombination. In a nanowire with approximately uniform thickness, the naïve assumption would be that counts should be generated uniformly across the nanowire. Instead, it is clear that the integrated counts drop both at the edge of the nanowire and in the vicinity of peaks in DE1. This trend indicates that both the nanowire surface and defects within the nanowire provide nonradiative recombination routes, in addition to the radiative recombination generating CL counts associated with these features. Quantum efficiency drops at regions of increased visible luminescence (defects), a poor prospect for optical ZnO devices operating in the visible spectrum, as nonradiative processes will reduce photoemission.

High-resolution STEM-CL mapping of ZnO nanowires can resolve variations both axial and perpendicular to growth axis, allowing structural features and luminescence signals to be related. This powerful characterization technique provides nanoscopic insight into luminescence processes and how they correlate locally to defects. In this Letter, we present high-resolution hyperspectral maps of a single nanowire by STEM-CL. However, simple mapping of the CL emission at different energies does not distinguish all of the underlying processes because their luminescence signatures overlap. Ensemble PL measurements can help to identify the key spectral features present within the sample (i.e., peak energy and spectral width), allowing them to be spectrally deconvolved from the noisier CL data. Maps of these components across a single nanowire identify an exciton diffusion length of ~50 nm and show that the dominant NBE luminescence is confined to the core of the nanowire and is suppressed near the surface (S) or defect sites (DE1, most likely zinc interstitials). Because the integrated intensity drops both at the surface and close to regions where DE1 is particularly bright, nonradiative recombination must occur at these locations at increased rates. A hierarchy of time scales (including trapping and recombination processes) can be established by considering the local suppression of different luminescence mechanisms. The excitation recombination timescale is longer than time scales associated with DE1 emission, which are, in turn, longer

than time scales associated with S luminescence. These different time scales arise from different lifetimes and trapping times associated with different luminescence processes and can be measured by complementary techniques such as transient absorption spectroscopy.

Spatial information about the distribution of defects will aid detailed simulations of ZnO nanostructures, providing a better understanding of consequent device properties. For example, band structure calculations may shed light on transport or photocatalysis, whereas the spatial distribution of optically active defects may inform how such nanostructures are deployed as optical gain media. The general STEM-CL approach may be more widely applied in the future to study other nanowire systems developed for optoelectronics or photocatalytic applications, in particular, those with in-built heterostructures or junctions. Improvements in optical detection will increase the spatial resolution of the CL signal and reduce exposure times. Future measurements may combine atomic-resolution TEM or STEM imaging of defect structures or other analytical techniques with high-resolution CL to establish definitive assignments that, despite significant work, are still controversial in ZnO.

## ■ ASSOCIATED CONTENT

### Supporting Information

The Supporting Information is available free of charge on the ACS Publications website at DOI: [10.1021/acs.jpclett.8b03286](https://doi.org/10.1021/acs.jpclett.8b03286).

Further details on the nanowire growth, nanowire geometry, nanowire PL and CL fitting, measurements on additional nanowires, CL deconvolution including maps of fitting errors, and CL line scans perpendicular to nanowire axis (PDF).

## ■ AUTHOR INFORMATION

### Corresponding Author

\*E-mail: [m.shaffer@imperial.ac.uk](mailto:m.shaffer@imperial.ac.uk).

### ORCID

Oscar W. Kennedy: 0000-0002-1945-960X

Charlotte K. Williams: 0000-0002-0734-1575

Milo S. P. Shaffer: 0000-0001-9384-9043

### Author Contributions

\*O.W.K. and E.R.W. contributed equally to this work.

### Notes

The authors declare no competing financial interest.

## ■ ACKNOWLEDGMENTS

The authors gratefully acknowledge financial support from EPSRC grant reference EP/K035274/1 (M.S.P.S. and E.R.W.) and EP/H005544/1 (P.A.W. and O.W.K.).

## ■ REFERENCES

- (1) Hadis, M.; Özgür, Ü. *Zinc Oxide: Fundamentals, Materials and Device Technology*; John Wiley & Sons: Hoboken, NJ, 2008.
- (2) Kind, B. H.; Yan, H.; Messer, B.; Law, M.; Yang, P. Nanowire Ultraviolet Photodetectors and Optical Switches. *Adv. Mater.* **2002**, *14* (2), 158–160.
- (3) Huang, M. H.; Mao, S.; Feick, H.; Yan, H.; Wu, Y.; Kind, H.; Weber, E.; Russo, R.; Yang, P. Room-Temperature Ultraviolet Nanowire Nanolasers. *Science* **2001**, *292* (5523), 1897–1899.
- (4) Plank, N. O. V.; Howard, I.; Rao, A.; Wilson, M. W. B.; Ducati, C.; Mane, R. S.; Bendall, J. S.; Louca, R. R. M.; Greenham, N. C.;

- Miura, H.; et al. Efficient ZnO Nanowire Solid-State Dye-Sensitized Solar Cells Using Organic Dyes and Core - Shell Nanostructures. *J. Phys. Chem. C* **2009**, *113* (43), 18515–18522.
- (5) Wan, Q.; Li, Q. H.; Chen, Y. J.; Wang, T. H.; He, X. L.; Li, J. P.; Lin, C. L. Fabrication and Ethanol Sensing Characteristics of ZnO Nanowire Gas Sensors. *Appl. Phys. Lett.* **2004**, *84* (18), 3654.
- (6) Soudi, A.; Hsu, C.-H.; Gu, Y. Diameter-Dependent Surface Photovoltage and Surface State Density in Single Semiconductor Nanowires. *Nano Lett.* **2012**, *12*, 5111–5116.
- (7) Jones, F.; Léonard, F.; Talin, A. A.; Bell, N. S. Electrical Conduction and Photoluminescence Properties of Solution-Grown ZnO Nanowires. *J. Appl. Phys.* **2007**, *102* (1), No. 014305.
- (8) Kolmakov, A.; Moskovits, M. Chemical Sensing and Catalysis By One-Dimensional Metal-Oxide Nanostructures. *Annu. Rev. Mater. Res.* **2004**, *34* (1), 151–180.
- (9) Law, M.; Kind, H.; Messer, B.; Kim, F.; Yang, P. Photochemical Sensing of NO<sub>2</sub> with SnO<sub>2</sub> Nanoribbon Nanosensors at Room Temperature. *Angew. Chem., Int. Ed.* **2002**, *41* (13), 2405–2408.
- (10) Madou, M. J.; Morrison, S. R. *Chemical Sensing with Solid State Devices*; Elsevier: Amsterdam, 2012.
- (11) Miller, D. R.; Akbar, S. A.; Morris, P. A. Nanoscale Metal Oxide-Based Heterojunctions for Gas Sensing: A Review. *Sens. Actuators, B* **2014**, *204* (July), 250–272.
- (12) Djurišić, A. B.; Leung, Y. H. Optical Properties of ZnO Nanostructures. *Small* **2006**, *2* (8–9), 944–961.
- (13) Djurišić, A. B.; Leung, Y. H.; Tam, K. H.; Hsu, Y. F.; Ding, L.; Ge, W. K.; Zhong, Y. C.; Wong, K. S.; Chan, W. K.; Tam, H. L.; et al. Defect Emissions in ZnO Nanostructures. *Nanotechnology* **2007**, *18* (9), No. 095702.
- (14) Liao, Z.-M.; Zhang, H.-Z.; Zhou, Y.-B.; Xu, J.; Zhang, J.-M.; Yu, D.-P. Surface Effects on Photoluminescence of Single ZnO Nanowires. *Phys. Lett. A* **2008**, *372* (24), 4505–4509.
- (15) Cross, R. B. M.; De Souza, M. M.; Narayanan, E. M. S. A Low Temperature Combination Method for the Production of ZnO Nanowires. *Nanotechnology* **2005**, *16* (10), 2188–2192.
- (16) Studenikin, S. A.; Golego, N.; Cocivera, M. Fabrication of Green and Orange Photoluminescent, Undoped ZnO Films Using Spray Pyrolysis. *J. Appl. Phys.* **1998**, *84* (4), 2287–2294.
- (17) Gong, Y.; Andelman, T.; Neumark, G. F.; O'Brien, S.; Kuskovsky, I. L. Origin of Defect-Related Green Emission from ZnO Nanoparticles: Effect of Surface Modification. *Nanoscale Res. Lett.* **2007**, *2* (6), 297–302.
- (18) Hsu, N. E.; Hung, W. K.; Chen, Y. F. Origin of Defect Emission Identified by Polarized Luminescence from Aligned ZnO Nanorods. *J. Appl. Phys.* **2004**, *96* (8), 4671–4673.
- (19) Sarkar, K.; Mukherjee, S.; Wiederrecht, G.; Schaller, R. D.; Gosztola, D. J.; Strosio, M. A.; Dutta, M. Ultrafast Carrier Dynamics and Optical Pumping of Lasing from Ar-Plasma Treated ZnO Nanoribbons. *Nanotechnology* **2018**, *29* (9), No. 095701.
- (20) Wang, J.; An, X.; Li, Q.; Egerton, R. F. Size-Dependent Electronic Structures of ZnO Nanowires. *Appl. Phys. Lett.* **2005**, *86* (20), 201911.
- (21) Fabbri, F.; Villani, M.; Catellani, A.; Calzolari, A.; Cicero, G.; Calestani, D.; Calestani, G.; Zappettini, A.; Dierre, B.; Sekiguchi, T.; et al. Zn Vacancy Induced Green Luminescence on Non-Polar Surfaces in ZnO Nanostructures. *Sci. Rep.* **2015**, *4* (1), 5158.
- (22) Mahfoud, Z.; Dijkman, A.; Javaux, C.; Bassoul, P.; Baudrion, A.; Plain, J.; Dubertret, B.; Kociak, M. Cathodoluminescence in a Scanning Transmission Electron Microscope: A Nanometer-Scale Counterpart of Photoluminescence for the Study of II – VI Quantum Dots. *J. Phys. Chem. Lett.* **2013**, *4* (23), 4090–4094.
- (23) Miller, D. R.; Williams, R. E.; Akbar, S. A.; Morris, P. A.; McComb, D. W. STEM-Cathodoluminescence of SnO<sub>2</sub> Nanowires and Powders. *Sens. Actuators, B* **2017**, *240*, 193–203.
- (24) Kociak, M.; Zagonel, L. F. Cathodoluminescence in the Scanning Transmission Electron Microscope. *Ultramicroscopy* **2017**, *176*, 112–131.
- (25) Liu, W.; Liang, Y.; Xu, H.; Wang, L.; Zhang, X.; Liu, Y.; Hark, S. Heteroepitaxial Growth and Spatially Resolved Cathodoluminescence of ZnO/MgZnO Coaxial Nanorod Arrays. *J. Phys. Chem. C* **2010**, *114* (39), 16148–16152.
- (26) Schirra, M.; Reiser, A.; Prinz, G. M.; Ladenburger, A.; Thonke, K.; Sauer, R. Cathodoluminescence Study of Single Zinc Oxide Nanopillars with High Spatial and Spectral Resolution. *J. Appl. Phys.* **2007**, *101* (11), 113509.
- (27) Zagonel, L. F.; Mazzucco, S.; Tence, March, K.; Bernard, R.; Laslier, B.; Jacopin, G.; Tchernycheva, M.; Rigutti, L.; Julien, F. H.; et al. Nanometer Scale Spectral Imaging of Quantum Emitters in Nanowires and Its Correlation to Their Atomically Resolved Structure. *Nano Lett.* **2011**, *11* (2), 568–573.
- (28) Bertoni, G.; Fabbri, F.; Villani, M.; Lazzarini, L.; Turner, S.; Van Tendeloo, G.; Calestani, D.; Gradečak, S.; Zappettini, A.; Salvati, G. Nanoscale Mapping of Plasmon and Exciton in ZnO Tetrapods Coupled with Au Nanoparticles. *Sci. Rep.* **2016**, *6*, 1–8.
- (29) Sutter, P.; Argyropoulos, C.; Sutter, E. Germanium Sulfide Nano-Optics Probed by STEM-Cathodoluminescence Spectroscopy. *Nano Lett.* **2018**, *18*, 4576–4583.
- (30) Kennedy, O. W.; Coke, M. L.; White, E. R.; Shaffer, M.; Warburton, P. A. MBE Growth and Morphology Control of ZnO Nanobelts with Polar Axis Perpendicular to Growth Direction. *Mater. Lett.* **2018**, *212*, 51–53.
- (31) Evans, S. M.; Giles, N. C.; Halliburton, L. E.; Kappers, L. A. Further Characterization of Oxygen Vacancies and Zinc Vacancies in Electron-Irradiated ZnO. *J. Appl. Phys.* **2008**, *103* (4), 043710.
- (32) Batson, P. E.; Reyes-Coronado, A.; Barrera, R. G.; Rivacoba, A.; Echenique, P. M.; Aizpurua, J. Plasmonic Nanobilliards: Controlling Nanoparticle Movement Using Forces Induced by Swift Electrons. *Nano Lett.* **2011**, *11* (8), 3388–3393.
- (33) Warmack, R. J.; Becker, R. S.; Anderson, V. E.; Ritchie, R. H.; Chu, Y. T.; Little, J.; Ferrell, T. L. Surface-Plasmon Excitation during Aloof Scattering of Low-Energy Electrons in Micropores in a Thin Metal Foil. *Phys. Rev. B: Condens. Matter Mater. Phys.* **1984**, *29* (8), 4375–4381.
- (34) Zutter, B.; Mecklenburg, M.; Regan, B. C. Aloof Beam Plasmons in Silver Nanoparticles. *Microsc. Microanal.* **2016**, *22* (S3), 1642–1643.
- (35) Kong, Y. C.; Yu, D. P.; Zhang, B.; Fang, W.; Feng, S. Q. Ultraviolet-Emitting ZnO Nanowires Synthesized by a Physical Vapor Deposition Approach. *Appl. Phys. Lett.* **2001**, *78* (4), 407.
- (36) Lyu, S. C.; Zhang, Y.; Ruh, H.; Lee, H.; Shim, H.; Suh, E.; Lee, C. J. Low Temperature Growth and Photoluminescence of Well-Aligned Zinc Oxide Nanowires. *Chem. Phys. Lett.* **2002**, *363* (1–2), 134–138.
- (37) Srikant, V.; Clarke, D. R. On the Optical Band Gap of Zinc Oxide. *J. Appl. Phys.* **1998**, *83* (10), 5447.
- (38) Misra, P.; Sharma, T. K.; Kukreja, L. M. Temperature Dependent Photoluminescence Processes in ZnO Thin Films Grown on Sapphire by Pulsed Laser Deposition. *Curr. Appl. Phys.* **2009**, *9* (1), 179–183.
- (39) Djurišić, A. B.; Choy, W. C. H.; Roy, V. A. L.; Leung, Y. H.; Kwong, C. Y.; Cheah, K. W.; Gundu Rao, T. K.; Chan, W. K.; Fei Lui, H.; Surya, C. Photoluminescence and Electron Paramagnetic Resonance of ZnO Tetrapod Structures. *Adv. Funct. Mater.* **2004**, *14* (9), 856–864.
- (40) Montenegro, D. N.; Hortelano, V.; Martínez, O.; Martínez-Tomas, M. C.; Sallet, V.; Muñoz-Sanjose, V.; Jiménez, J. Non-Radiative Recombination Centres in Catalyst-Free ZnO Nanorods Grown by Atmospheric-Metal Organic Chemical Vapour Deposition. *J. Phys. D: Appl. Phys.* **2013**, *46* (23), 235302.
- (41) Mooney, J.; Kambhampati, P. Get the Basics Right: Jacobian Conversion of Wavelength and Energy Scales for Quantitative Analysis of Emission Spectra. *J. Phys. Chem. Lett.* **2013**, *4*, 3316–3318.
- (42) Cui, M.; Zhang, Z.; Wang, Y.; Finch, A.; Townsend, P. D. Temperature Dependence of Bulk Luminescence from ZnO. *Luminescence* **2018**, *33* (4), 654–659.
- (43) Donatini, F.; De Luna Bugallo, A.; Tchoulfan, P.; Chicot, G.; Sartet, C.; Sallet, V.; Pernot, J. Comparison of Three E-Beam Techniques for Electric Field Imaging and Carrier Diffusion Length

Measurement on the Same Nanowires. *Nano Lett.* **2016**, *16* (5), 2938–2944.

(44) Hwang, J. S.; Donatini, F.; Pernot, J.; Thierry, R.; Ferret, P.; Dang, L. S. Carrier Depletion and Exciton Diffusion in a Single ZnO Nanowire. *Nanotechnology* **2011**, *22* (47), 475704.

(45) Mehl, B. P.; Kirschbrown, J. R.; Gabriel, M. M.; House, R. L.; Papanikolas, J. M. Pump – Probe Microscopy: Spatially Resolved Carrier Dynamics in ZnO Rods and the Influence of Optical Cavity Resonator Modes. *J. Phys. Chem. B* **2013**, *117* (16), 4390–4398.

(46) Lin, Y.; Wang, D.; Zhao, Q.; Li, Z.; Ma, Y.; Yang, M. Influence of Adsorbed Oxygen on the Surface Photovoltage and Photoluminescence of ZnO Nanorods. *Nanotechnology* **2006**, *17* (9), 2110–2115.

(47) Fabbri, F.; Villani, M.; Catellani, A.; Calzolari, A.; Cicero, G.; Calestani, D.; Calestani, G.; Zappettini, A.; Dierre, B.; Sekiguchi, T.; et al. Zn Vacancy Induced Green Luminescence on Non-Polar Surfaces in ZnO Nanostructures. *Sci. Rep.* **2015**, *4* (1), 5158.

(48) Liberti, E.; Menzel, R.; Shaffer, M. S. P.; McComb, D. W. Probing the Size Dependence on the Optical Modes of Anatase Nanoplatelets Using STEM-EELS. *Nanoscale* **2016**, *8* (18), 9727–9735.

(49) Huang, M. R. S.; Erni, R.; Lin, H. Y.; Wang, R. C.; Liu, C. P. Characterization of Wurtzite ZnO Using Valence Electron Energy Loss Spectroscopy. *Phys. Rev. B: Condens. Matter Mater. Phys.* **2011**, *84* (15), 155203.

(50) McCluskey, M. D.; Jokela, S. J. Defects in ZnO. *J. Appl. Phys.* **2009**, *106* (7), 071101.